Journal of Materials Science: Materials in Electronics
https://doi.org/10.1007/s10854-019-01330-z

Structural, optical, and electrical evolution of sol–gel-immersion grown nickel oxide nanosheet array films on aluminium doping

M. H. Mamat[1,2] · **N. Parimon**[1] · **A. S. Ismail**[1] · **I. B. Shameem Banu**[3] · **S. Sathik Basha**[3] · **G. V. Vijayaraghavan**[3] · **M. K. Yaakob**[4] · **A. B. Suriani**[5] · **M. K. Ahmad**[6] · **M. Rusop**[1,2]

Received: 15 January 2019 / Accepted: 11 April 2019

Abstract

We developed aluminium (Al)-doped nickel oxide (NiO) nanosheet arrays film on the indium-doped tin oxide (ITO) substrate via sol–gel immersion method using nickel nitrate hexahydrate and aluminium nitrate nonahydrate as precursor and dopant materials, respectively. The Al-doping concentrations were varied from 0 to 2 at.%. Uniform Al-doped NiO nanosheet array films were observed on the substrate; the denser and smaller size of the NiO nanosheets were obtained at higher Al-doping concentrations. The growth mechanism was proposed. The crystallinity of Al-doped NiO nanosheet deteriorated at higher doping concentration. Meanwhile, the crystallite size, lattice parameter, and interplanar spacing were reduced with the doping quantity. The compressive strain, tensile stress, dislocation density, and band gap of the Al-doped NiO upsurged at higher doping concentration. The current–voltage measurement results revealed that the resistivity increased after the doping process up to 2 at.%. The Raman spectra showed that the doped samples exhibit blue-shift and decreased intensity of the Raman peaks.

1 Introduction

Nanostructured oxides such as zinc oxide (ZnO), titanium dioxide (TiO_2), niobium pentaoxide (Nb_2O_5) and nickel oxide (NiO) have been utilized in the several technical areas including solar cells, sensors, batteries, photocatalyst, and smart coatings [1–6]. These materials possess tremendous characteristics although in the pristine condition, and their characteristics could be further fine-tuned and enhanced based on different applications. Among these nanostructured metal oxides, NiO as a transition metal oxide provides huge potential for various applications including supercapacitor, sensors, and photocatalyst [7–9]. In addition, NiO has several potential applications particularly for packaging materials, batteries, wide-electromagnetic absorbers, and wastewater catalysts when composited with polymers and other metal oxides [10–14]. NiO belongs to p-type semiconductor category, which has wide band gap of 3.6 to 4.0 eV. NiO also has prominent electrical and electronic properties and outstanding chemical stability. However, as a p-type material, NiO properties and their characteristic tunings are still at the early stage to be understood as compared to the n-type materials, particularly for applications in electronic devices. Therefore, more systematic studies are required to produce NiO nanostructured with desired properties and perhaps these NiO nanostructures with enhanced performance could become alternative materials to n-type semiconductors for various applications in the near future.

To improve NiO characteristics, there are several effective approaches have been reported by other researchers to suit different applications. For example, NiO nanostructures have been constructed in numerous complex shapes

---

✉ M. H. Mamat
mhmamat@uitm.edu.my

[1] NANO-ElecTronic Centre (NET), Faculty of Electrical Engineering, Universiti Teknologi MARA (UiTM), 40450 Shah Alam, Selangor, Malaysia

[2] NANO-SciTech Centre (NST), Institute of Science (IOS), Universiti Teknologi MARA (UiTM), 40450 Shah Alam, Selangor, Malaysia

[3] Department of Physics, B.S. Abdur Rahman Crescent Institute of Science & Technology, Vandalur, Chennai 600 048, India

[4] Faculty of Applied Sciences, Universiti Teknologi MARA (UiTM), 40450 Shah Alam, Selangor, Malaysia

[5] Nanotechnology Research Centre, Faculty of Science and Mathematics, Universiti Pendidikan Sultan Idris (UPSI), 35900 Tanjung Malim, Perak, Malaysia

[6] Microelectronic and Nanotechnology – Shamsuddin Research Centre (MiNT-SRC), Faculty of Electrical and Electronic Engineering, Universiti Tun Hussein Onn Malaysia (UTHM), 86400 Batu Pahat, Johor, Malaysia

to produce unique characteristics, and have been coated with various metals particularly noble metal, which show improvement in the sensing and surface catalytic properties [2, 15]. In addition, some of the researchers have reported on upgraded performance of NiO when the NiO is composited with other materials such as manganese oxide and reduced graphene oxide [16, 17]. Doping process is also considered as an efficient method to produce NiO nanostructures with improved properties. Besides, this doping process is regarded to be one of the most simplistic and dependable methods to modify the optical, structural, and electrical properties, thus stimulating the improved performance for the NiO-based applications. So far, NiO have been doped with numerous metals such as magnesium (Mg), zinc (Zn), cadmium (Cd), tin (Sn), and aluminum (Al) [18–21]. However, most of the doping processes were conducted on powder form NiO structures and granular-type NiO films. Meanwhile, the report on doping process of NiO nanostructures thin films are still lacking. Various techniques such as electrochemical, sputtering, sol gel process, and spray pyrolysis have been utilized to deposit or to grow NiO nanostructures in films or powder forms [22–25]. Among these methods, the sol–gel process is chosen in this research due to its effectiveness both in cost and material processing to produce NiO nanostructures with good quality.

Accordingly, in the present work, pristine and Al-doped NiO nanosheet array films with different dopant concentrations were grown on the indium-doped tin oxide (ITO) glass substrate by low temperature sol–gel immersion approach. This technique is contemplated as a facile route to grow nanosheet array, with excellent controllability of dopant and precursor material compositions. The NiO nanosheet structures were grown on ITO glass substrate because the substrate had been widely used as a transparent conducting oxides for various devices such as sensors and solar cells. The ITO glass substrate also has high optical transparency in the visible region and low resistivity approaching that of a metal, which could be utilized as Ohmic contact to the semiconductors. Previous studies have been focused on granular-type NiO thin films and their structural and optical properties has been discussed in details. In addition, the NiO nanostructures in powder form has been discussed substantially in the literatures. However, the details study involving NiO nanosheet array films, which are directly grown onto the ITO substrate through one-step sol–gel immersion process, particularly after doping process with Al has been rarely reported in the literatures. This study perhaps will provide important insight into the structural, optical, and electrical characteristics of the grown Al-doped NiO nanosheet array films on the ITO for electronic devices application. Furthermore, the behaviour of Al-doped NiO nanosheet array films on the ITO at different Al concentration could be understood and predicted for the applications in the electronic device as well for the device performance tuning.

2 Experimental procedure

Al-doped NiO nanosheet films were grown on the ITO glass substrates using sol–gel immersion method. The ITO glass substrate, which has resistivity of 15 Ω cm and ITO layer thickness of approximately 200 nm, was commercially purchased. The solutions to grow Al-doped NiO nanosheet arrays at different doping concentrations were prepared using nickel (II) nitrate hexahydrate ($Ni(NO_3)_2•6H_2O$), aluminium (III) nitrate nonahydrate ($Al(NO_3)_3•9H_2O$), and hexamethylenetetramine (HMT, $C_6H_{12}N_4$) as precursor, dopant source, and stabilizer, respectively. These reagents were mixed into a beaker, in which deionized (DI) water was filled inside. The concentrations of precursor and stabilizer were fixed at 0.1 M. Meanwhile, the Al dopant concentrations were varied to achieve 0, 0.2, 0.4, 0.6, 0.8, 1.0, and 2.0 at.% based on molar ratio to the precursor. Then, the solutions with different doping concentrations were sonicated for 5 min by ultrasonic bath (Hwasin Technology Powersonic 405, 40 kHz) in order to improve the solution's miscibility and homogeneity. Subsequently, these solutions were poured into the Schott bottles. Inside the bottles, the ITO glass substrates were placed at the bottom, where the conducting side of the substrate was facing upward. Then, these Schott bottles were kept inside an electric oven. The chemical reactions for the Al-doped NiO nanosheet growth process was carried out at 120 °C for 2 h inside the oven. After the growth process, all synthesized samples (on ITO substrate) were rinsed by DI water and baked at 150 °C for 10 min. Subsequently, the samples were annealed at 500 °C for 1 h using a thermal box furnace. The process flow of Al-doped NiO nanosheet films is shown in Fig. 1. The resulting Al-doped NiO nanosheet array films which were grown at Al concentrations of 0 (undoped), 0.2, 0.4, 0.6, 0.8, 1.0, and 2.0 at.% have been labelled by ANO1, ANO2, ANO3, ANO4, ANO5, ANO6, and ANO7, respectively.

The morphologies and cross sectional images of the grown Al-doped NiO nanosheet with porous structures were investigated by field-emission scanning electron microscopy (FESEM, JEOL JSM-7600F). The elemental analysis of the doped sample was conducted using energy dispersive X-ray spectroscopy (EDX, Inca). The crystal structures and structural properties of the samples were carried out using X-ray diffraction (XRD, PANalytical X'pert PRO). The structural properties of the films were also investigated by using Raman spectroscopy (Horiba Jobin-Yvon-79 DU420A-OE-325, 514 nm Ar laser). The transmittance and optical properties of the grown Al-doped NiO nanosheet films were characterized by ultraviolet–visible (UV–Vis) spectroscopy

Fig. 1 Schematic of process flow to grow Al-doped NiO nanosheet array film on ITO glass substrate

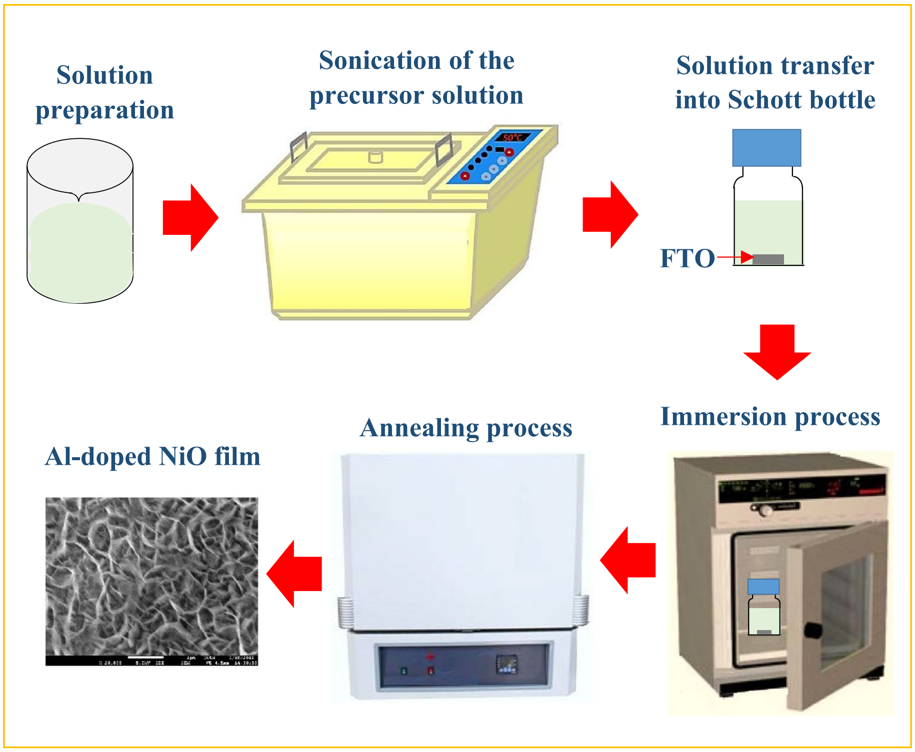

(Perkin-Elmer Lambda 750). The current–voltage (I–V) measurement plots were attained by using two-probe I–V measurement system (Keysight B1500A). In order to measure the I–V, platinum (Pt) electrodes were deposited on the surface of the sample using a thermal evaporator (Ulvac) at thickness of 60 nm. A physical mask was used to create an electrode pattern on the samples.

3 Result and discussion

The FESEM surface morphologies images of ANO1 to ANO7 are presented in Fig. 2a–n. From the FESEM images, the pristine ANO1 is grown well on the ITO substrate with nanosheet architectures. These nanosheets combined each other to form highly porous nanosheet network film. The nanosheets for pristine ANO1 are very large and have asymmetrical shape. The observation from the FESEM images also reveals that numerous mesopores are disseminated on the film's surface. However, when the NiO nanosheet is doped with Al at 0.2 at.% as represented by ANO2 in Fig. 2b, the significant morphology changes are observed, whereby the individual nanosheet exhibits reduction in size and irregularity to form film networking. The film of ANO2 also demonstrates more uniform and smoother nanosheet structures than those grown without Al-doping. This sample also showed a denser mesoporous nanosheet array architecture than that of pristine ANO1. Further doping process at Al concentration of 0.4 at.%, which is depicted by ANO3 sample in Fig. 2c, produces smaller nanosheet structure grown on ITO as compared than that of the pristine ANO1 and 0.2 at.% doped sample of ANO2. In this ANO3 film, the growth of nanosheet structure seems to be deteriorated although the nanosheet linkage to each other still can be observed in the FESEM image. The formations of nanosheet are barely seen in ANO4, ANO5, ANO6, and ANO7 samples as the concentration of Al dopant was increased from 0.6 to 2 at.%, which are displayed in Fig. 2d–g, respectively. This condition was confirmed by observing the morphological images of these samples at higher magnification (at ×50,000 magnification) as shown in Fig. 2k–n, whereby the nanosheet growth in the vertical direction is deteriorated at higher doping concentration. The magnified FESEM images at ×50,000 magnification for ANO1 to ANO3 samples are also shown in Fig. 2h–j for reference and comparison. These results evidently show that the Al doping could modulate the density, size, and irregularity characteristics of the NiO nanosheets on ITO glass. From these observation, we believe that higher Al doping concentration does not favored the direct formation of NiO nanosheet array architectures on the ITO glass, although the doping process at higher Al doping concentration was reported to be successful for the NiO nanostructures in powder form [21, 26]. The growth of NiO nanosheets on the ITO glass is subjugated by self-assembly and oriented attachment mechanism. Generally, the formation of NiO nanosheets on the ITO could be expressed by the following chemical reactions [27, 28]:

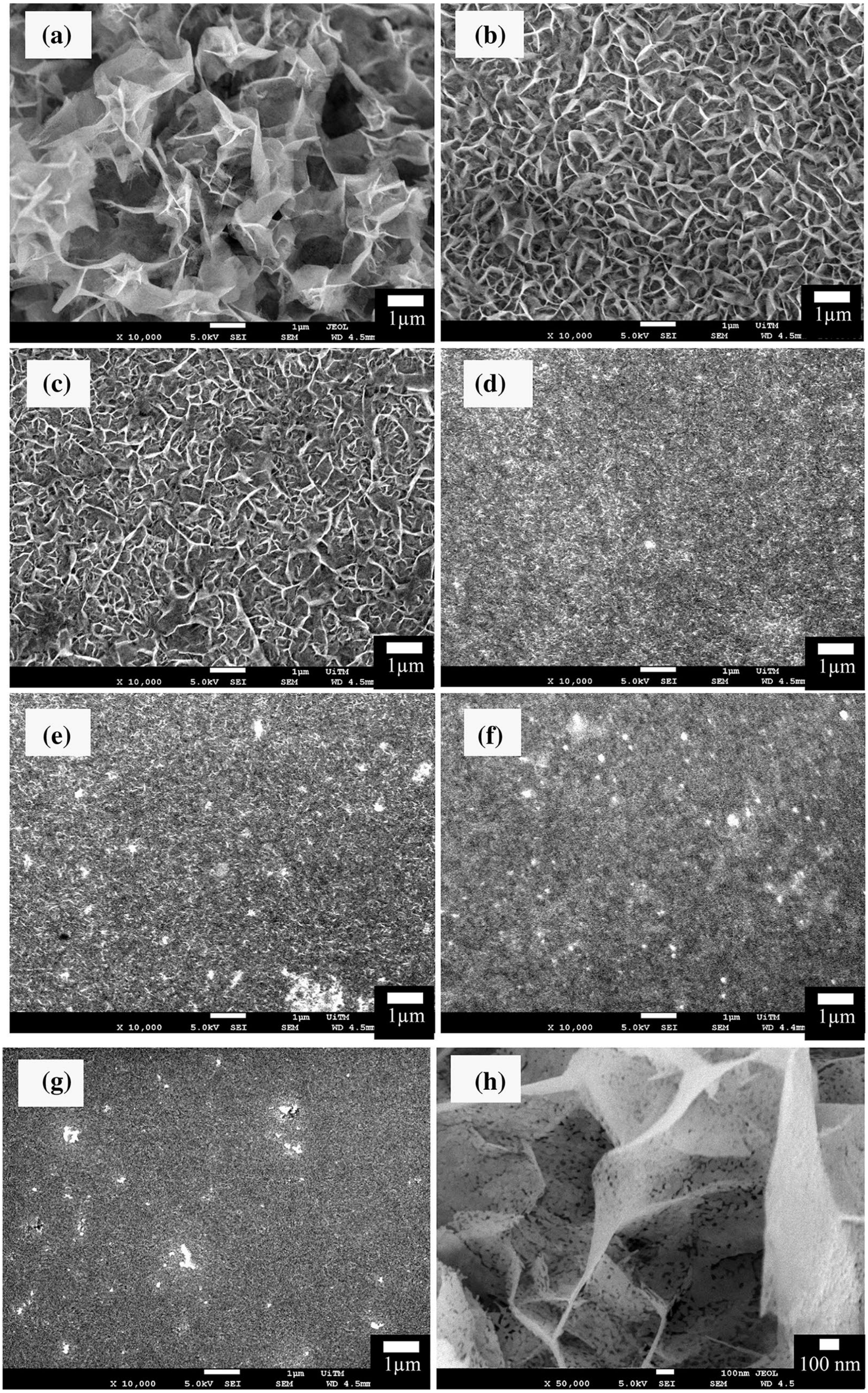

Fig. 2 The surface morphologies of **a** ANO1, **b** ANO2, **c** ANO3, **d** ANO4, **e** ANO5, **f** ANO6, and **g** ANO7 at magnification of ×10,000. Magnified FESEM images of **h** ANO1, **i** ANO2, **j** ANO3, **k** ANO4, **l** ANO5, **m** ANO6, and **n** ANO7 samples (at magnification of ×50,000)

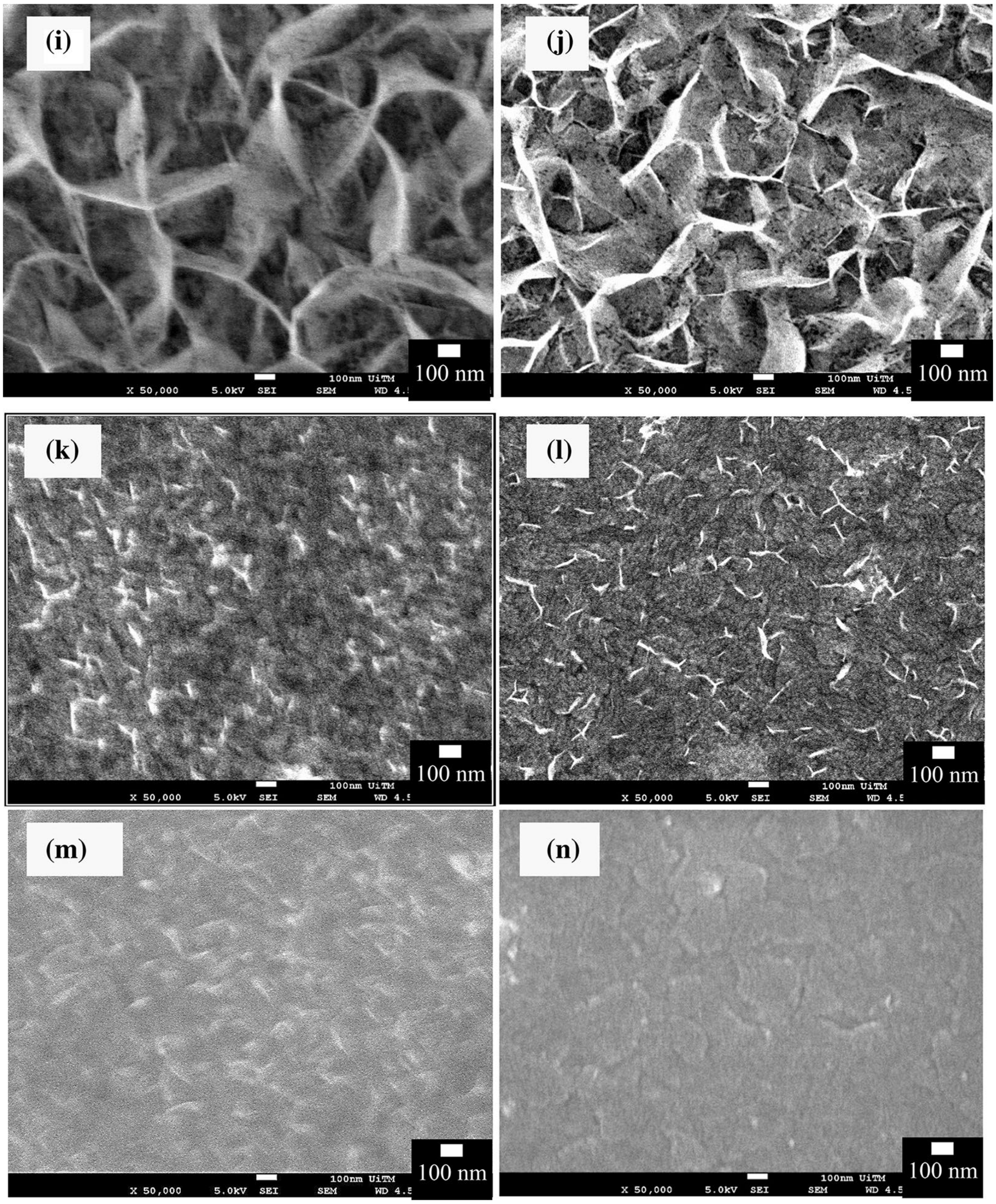

Fig. 2 (continued)

$$(CH_2)_6N_4 + 6H_2O \rightarrow 6HCHO + 4NH_3 \quad (1)$$

$$NH_3 + H_2O \rightarrow NH_4^+ + OH^- \quad (2)$$

$$Ni(NO_3)_2 \cdot 6H_2O \rightarrow Ni^{2+} + 2NO_3^- + 6H_2O \quad (3)$$

$$Ni^{2+} + 2OH^- + \chi H_2O \rightarrow Ni(OH)_2 \cdot \chi H_2O \quad (4)$$

$$Ni(OH)_2 \cdot \chi H_2O \rightarrow NiO \; + \; (\chi + 1)H_2O \quad (5)$$

and/or

$$Ni^{2+} + (2 - y)OH^- + yNO_3^- + \chi H_2O \rightarrow Ni(OH)_{2-y}(NO_3)_y \cdot \chi H_2O \quad (6)$$

$$Ni(OH)_{2-y}(NO_3)_y \cdot \chi H_2O \rightarrow NiO + (\chi + 1 - y)H_2O + yHNO_3 \quad (7)$$

The control of Ni^{2+} hydrolyzation is important to produce well-assembled nanosheets array structure. This process can be achieved by introduction of HMT in the solution. The HMT act as a pH buffer, which supplies hydroxide (OH^-) ion slowly to the reaction. Firstly, in this aqueous medium, the HMT reacts with water to produce formaldehyde (HCHO) and ammonia (NH_3) in the process as shown in Eq. (1). Next, the produced NH_3 reacts with water to form ammonium (NH_4^+) and OH^- ions, in which the reaction could be described in Eq. (2). Meanwhile, nickel nitrate hexahydrate dissolves in the

DI water to produce Ni^{2+} ion and other byproducts as shown in Eq. (3). The unreacted NH_3 from Eq. (1) could function as a surfactant agent to the Ni^{2+} ions, whereby the reaction between these two species forms complex NH_3–Ni molecules. These complex molecules decrease the concentration of Ni^{2+} ions in the solution, which modulate the growth rate of crystal [19]. As these chemical reactions continue, the hydrolyzation of HMT increases, which subsequently increases the concentration of OH^- in the solution. This condition is favorable for the growth and condensation of $Ni(OH)_2 \cdot \chi H_2O$ on the ITO as shown in Eq. (4). The remaining HMT molecules, which are not involved in the above mentioned reactions, may help to produce $Ni(OH)_2 \cdot \chi H_2O$ nanosheet structure by adsorbing on the certain planes of $Ni(OH)_2 \cdot \chi H_2O$ selectively, particularly on (001) plane due to its high binding potential. Due to this HMT adsorption, the growth along the (001) plane is inhibited, while allowing the growth occurs at other plane directions. Overtime, the thin two-dimensional nanosheet network layer is form on the ITO as indicated in Eq. (5). According to Meher et al. the nitrate ions may intercalates into condensed $Ni(OH)_2$ in the form of hydroxyl deficient to produce $Ni(OH)_{2-y}(NO_3)_y \cdot \chi H_2O$, where $y = 0.2–0.4$ and $\chi = 0.6–1$ [28]. During immersion and annealing process, the $Ni(OH)_2 \cdot \chi H_2O$ and/or $Ni(OH)_{2-y}(NO_3)_y \cdot \chi H_2O$ is converted into NiO and release other byproducts as suggested in the Eqs. (6) and (7). This NiO transformation can be completely performed at temperature 280 °C and above [29]. The film on the ITO substrate eventually turned from light green color to grey color after the annealing process, which suggests the oxidizing state and nonstoichiometry transformation of the film. In the presence of Al dopant ions, the formation of NiO nucleus is reduced because of the increased energy barrier based on the classical nucleation model. Furthermore, the Al^{3+} dopant ions may form complexes with OH^- ions to reduce OH^- ion concentrations in the solution. These conditions decrease the heterogeneous nucleation of NiO on the substrate. Therefore, thin and small nanosheet structures were observed for Al-doped NiO samples particularly when the Al concentrations are increased up to 2 at.%. Besides, the Al dopants may exist on the nanoflake surface at the early stage of nanosheet growth, which disturb the formation of NiO nanosheet particularly at high Al content. The enthalpy of formation for Al dopants to form oxide is -1676 kJ mol^{-1}, which are relatively smaller than that of NiO (-240 kJ mol^{-1}) [30–33]. Hence, the incorporation of Al dopants at an early stage of the nanosheet growth is plausible due to its low formation enthalpy, which may change the system's free energy. Consequently, the growth of nanosheet is retarded during immersion process when the Al content increases.

The cross-sectional images of undoped and Al-doped samples were observed using FESEM. Figure 3a–g displays cross-sectional images of ANO1 to ANO7, which were prepared at different Al contents. These images demonstrate that all NiO nanosheet arrays were grown on ITO-coated glass substrate with good coverage. The cross-sectional image of pristine ANO1 sample is shown in Fig. 3a. This image indicates that the sample contains large nanosheet arrays, which are stacked to each other forming 4243-nm-thick film in average. When the sample is doped with 0.2 at.% Al as represent by ANO2 sample, the average thickness of the film reduces to 3167 nm as displayed in Fig. 3b. The decrease of film thickness was also observed for ANO3, ANO4, ANO5, ANO6, and ANO7, with average film thicknesses of 1038, 327, 198, 146, and 83 nm, respectively. The cross-sectional images of ANO3, ANO4, ANO5, ANO6, and ANO7 samples are presented in Fig. 3c–g, respectively. This result indicates that the average thickness of NiO reduces as Al content is increased, which support the inhibition growth of NiO at higher Al content as discussed previously. The EDX analyses were performed on ANO2 and ANO7 samples, in which the results are shown in Fig. 3h and i, respectively. The EDX results indicate that Al dopant co-exists with Ni and O elements, with atomic ratio of 0.14 (Al), 19.39 (Ni), and 80.47 (O) recorded for ANO2, while for ANO7 the atomic ratio is shown as 1.78 (Al), 18.84 (Ni), and 79.38 (O). The other peaks, which are not labelled in the spectra, arose due to contribution of the ITO-glass substrate.

The XRD patterns of ANO1 to ANO7 are shown in Fig. 4. The pristine ANO1 sample showed well-resolved diffraction peaks at 37.71°, 43.78°, 63.30°, and 75.81°; these peaks can be indexed as the peaks corresponding to the (111), (200), (220), and (311) planes, respectively of face-centered cubic (fcc) NiO structure (JCPDS File Card No. 78-0643). The ITO (substrate) peaks were also observed and labelled with * symbol. However, the crystallinity of the Al-doped NiO nanosheet arrays of ANO2 to ANO7 decreased dramatically as the diffraction peaks intensity and full witdh at half maximum (FWHM) became lower and broader, respectively with increasing the Al doping amount. This condition indicates that Al inhibits the growth of NiO nanocrystals as can be observed in the morphological images in the Fig. 2. The increasing Al doping concentration also deteriorates the crystal cubic structure of NiO. At higher Al-doping amount, ionized Al dopant may capture more oxygen in competition with Ni ion due to its larger nuclear charge, which cause diminution of the NiO crystallinity. Other oxides such as aluminium oxide (Al_2O_3) or/and new spinnel phase of nickel aluminium oxide ($NiAl_2O_4$) may possibly formed in small quantity on the nanosheet surface and accumulated at the grain boundaries, which affects the crystalline properties of NiO. Because this oxide is in very small amount, it is very difficult to be observed in the XRD patterns and possibly the XRD may not sensitive enough to detect such low amounts of oxide. Similar observations of crystallinity degradation in NiO films also reported by other groups, when they doped NiO with Al, Fe, In, W, and Sn [34–39].

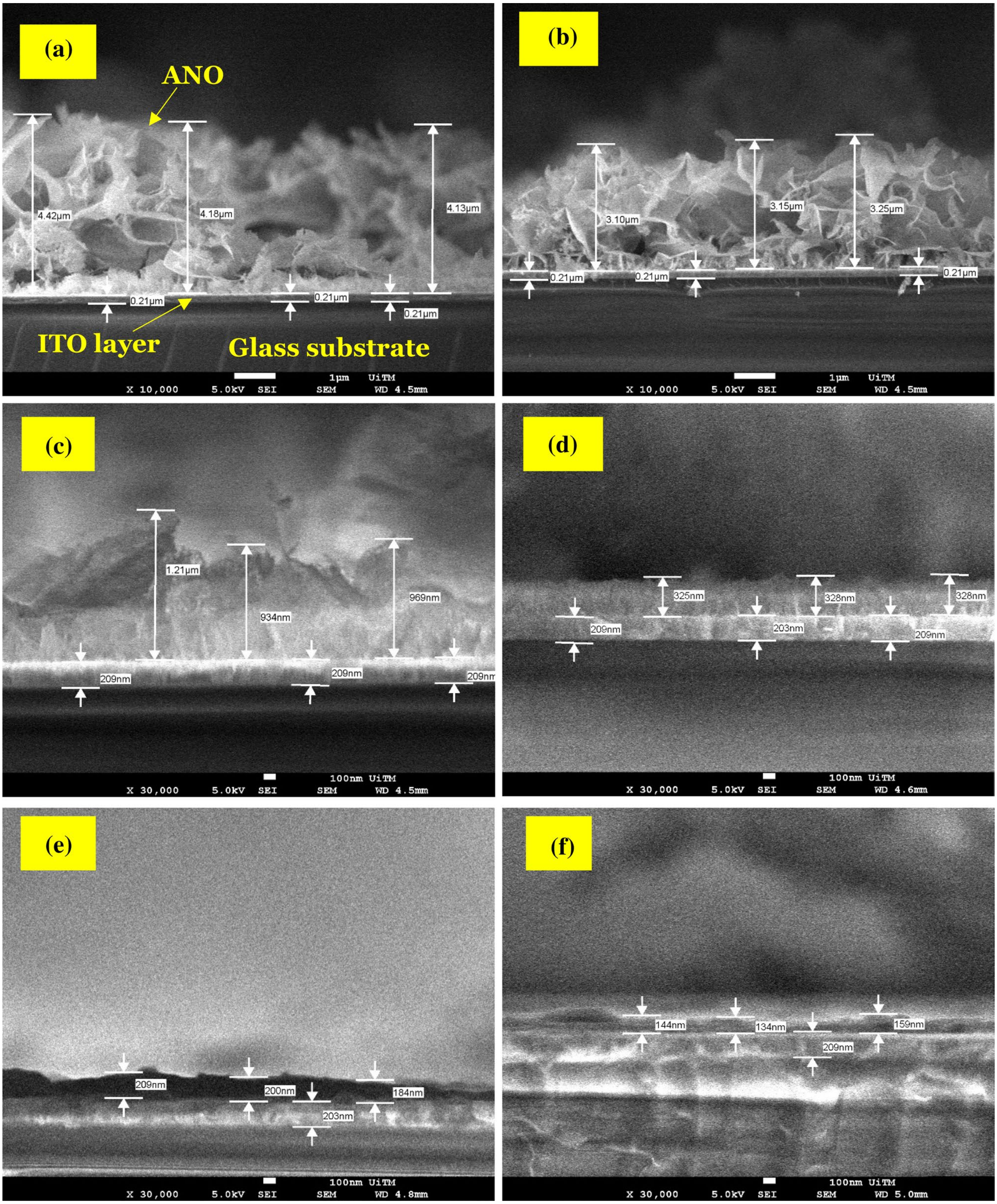

Fig. 3 The cross-sectional images of **a** ANO1, **b** ANO2, **c** ANO3, **d** ANO4, **e** ANO5, **f** ANO6, and **g** ANO7. EDX spectra of Al-doped NiO nanosheet arrays for **h** ANO2 and **i** ANO7 samples

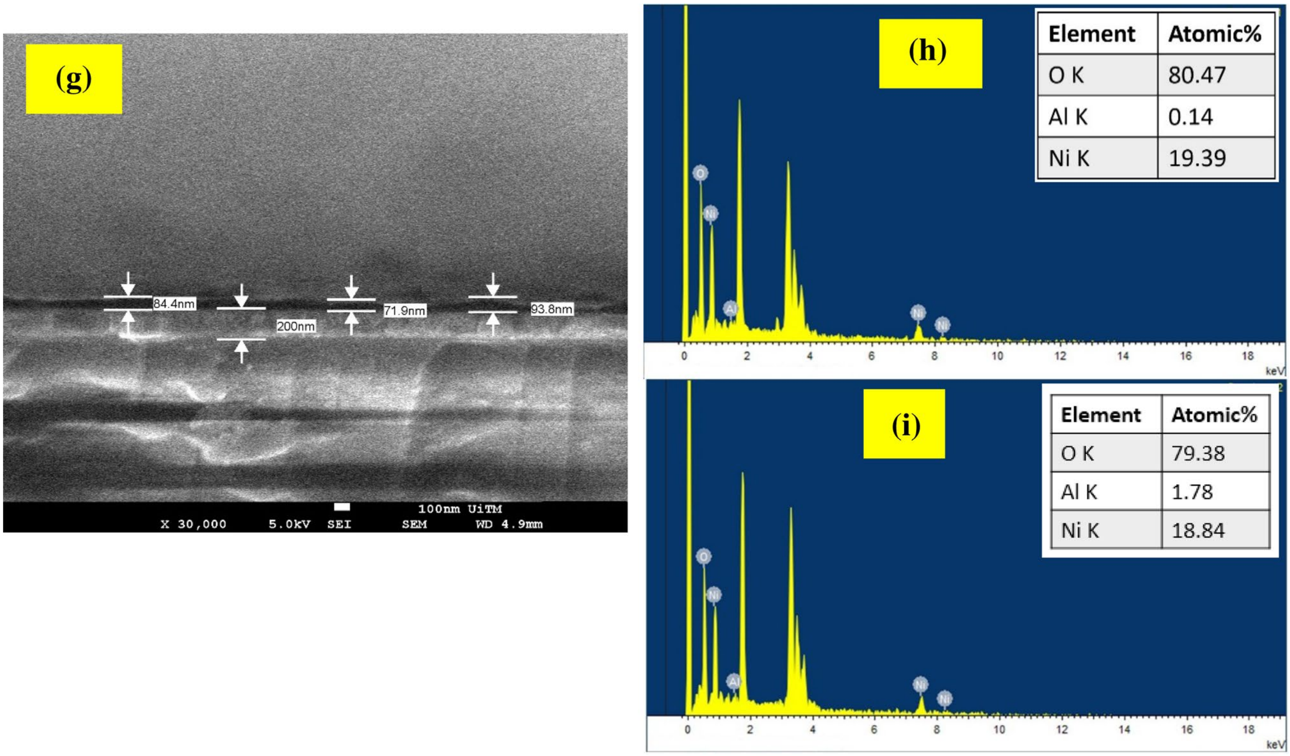

Element	Atomic%
O K	80.47
Al K	0.14
Ni K	19.39

Element	Atomic%
O K	79.38
Al K	1.78
Ni K	18.84

Fig. 3 (continued)

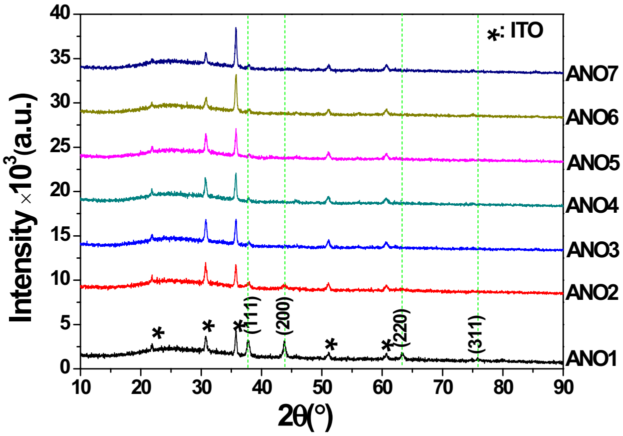

Fig. 4 XRD patterns of Al-doped NiO nanosheet films at different Al content

The average crystallite size (D) was estimated according to the Scherrer formula:

$$D = \frac{0.94\lambda}{\beta \cos\theta} \quad (8)$$

here β is the FWHM (in unit of radians), θ is the diffraction angle, and λ is the X-ray wavelength of 1.54 Å. The values of β and θ were acquired from (111) plane orientation and shown in Table 1. The calculated average crystallite sizes of the ANO1, ANO2, ANO3, ANO4, ANO5, ANO6, and ANO7 are approximately 50.5, 45.0, 39.9, 25.7, 24.4, 19.9, and 13.5 nm, respectively. Evidently, the increase of the Al doping amount leads to the decrease of NiO crystallite size. Therefore, the integration of Al ions into the lattice of NiO can be considered as conceivable.

The dislocation densities, δ of ANO1 to ANO7 were calculated based on the Williamson and Smallman's relation:

$$\delta = \frac{1}{D^2} \quad (9)$$

From this relation, it was found that the dislocation density vividly increases with the increased Al doping amount as shown in Table 1. This dislocation density parameter is related to the possible defaults and amount of crystal defects in the pristine and Al-doped films. This result suggests that incorporation of Al into NiO lattice triggered substantial local distortion, which represents by the increased dislocation density value at higher doping concentration.

The lattice parameter, a and interplanar distance, d of fcc NiO structure is estimated based on the following equations:

$$\frac{1}{d^2} = \frac{h^2 + k^2 + l^2}{a^2} \quad (10)$$

Table 1 2θ, FWHM, crystallite size, unit cell volume, lattice parameter, interplanar spacing, strain, stress, and dislocation density of ANO1 to ANO7 samples

Samples	2θ (°)	FWHM, β (°)	Crystallite size, D (nm)	Unit cell volume V (10^{-2}×nm^3)	Lattice parameter, a (nm)	Interplanar spacing, d (nm)	Strain, ε (%) (*negative sign indicates compressive strain)	Stress, σ (GPa)	Dislocation density, δ (Lines/m^2)
ANO1	37.71	0.174	50.5	7.06	4.1322	2.3857	− 1.08	3.47	3.93×10^{14}
ANO2	37.85	0.195	45.0	6.98	4.1174	2.3772	− 1.43	4.61	4.94×10^{14}
ANO3	37.88	0.220	39.9	6.96	4.1143	2.3754	− 1.50	4.85	6.28×10^{14}
ANO4	37.92	0.342	25.7	6.94	4.1101	2.3730	− 1.60	5.17	1.51×10^{15}
ANO5	37.94	0.360	24.4	6.93	4.1080	2.3718	− 1.65	5.33	1.68×10^{15}
ANO6	37.98	0.441	19.9	6.91	4.1039	2.3694	− 1.75	5.66	2.52×10^{15}
ANO7	38.04	0.653	13.5	6.88	4.0976	2.3658	− 1.90	6.14	5.52×10^{15}

$$d = \frac{n\lambda}{2\sin\theta} \tag{11}$$

here h, k and l are the Miller indices of the planes, and n is the order value of diffraction (usually n = 1). The calculated a and d of ANO1 to ANO7 are presented in Table 1. The result shows that the a and d of Al-doped NiO nanosheet arrays reduces as the Al doping amount increases, which can be explained by smaller ionic radii of Al^{3+} ion than that of Ni^{2+} ion. The ionic radii of Al^{3+} at a coordination number (CN) of 6 is 0.054 nm, respectively, which are smaller than that of Ni^{2+} at a CN of 6 (0.069 nm) [40, 41]. Based on the previous reports, the substitutional doping of Al into NiO is likely to happen because the ionic radii and charge state of Al^{3+} ions do not have significant difference as compared to that of Ni ions [21, 42–44]. Consequently, the lattice parameters decreased leading to upward shift of XRD diffraction peaks, which proved by the XRD analyses. The small ionic radii of Al^{3+} substituted in the Ni^{2+} site may form strain and local distortion in the NiO lattice. As a results of lattice constant a reduction with Al contents, the unit cell volume exhibits a decreased value as can be calculated by following equation:

$$V = a^3 \tag{12}$$

where a denotes the lattice constant of the grown samples. The obtained values for the unit cell volumes of the ANO1 to ANO7 are shown in Table 1. Subsequently, the reduced lattice constant a and interplanar spacing d also induced strain and stress in the films. The strain, ε and the stress, σ of the samples were analyzed by using Eq. 13 and Eq. 14, respectively as follows [45, 46]:

$$\varepsilon = \frac{a - a_0}{a_0} \times 100 \tag{13}$$

$$\sigma = \frac{-E(a - a_0)}{2a_0 p} \tag{14}$$

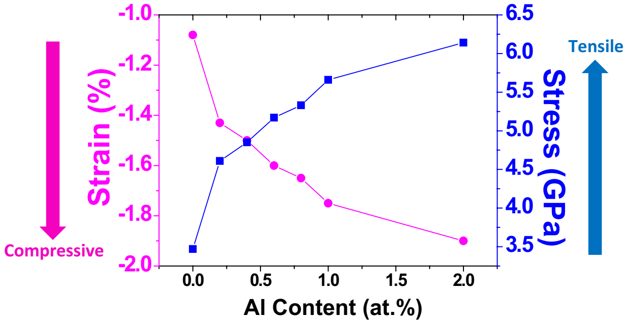

Fig. 5 Strain and stress characteristics of Al-doped NiO at various Al content

here a_0 is the lattice parameter of synthesized NiO, a_0 is the lattice constant of bulk NiO (a_0=4.1771), E is the Young's modulus (E_{NiO}= 200 GPa), and p is the Poisson ratio (p_{NiO}=0.31). For strain analysis, if the strain value is positive, the strain is considered as a tensile strain (positive value). In contrary, negative value of strain indicates that the strain is a compressive strain (negative value). Meanwhile, for the stress analysis, the positive and negative value of stress represent the tensile stress (positive value) and compressive stress (negative value), respectively. The calculated results are shown in Fig. 5 and Table 1, which suggest that both compressive strain and tensile stress increase with the increased Al-doping. This may be attributed to the difference of ionic radii between Al^{3+} and Ni^{2+} ions, which leads to an internal distortion in the host lattice. Subsequently, this condition disturbs the crystalline nature of NiO and then stimulates the defects formation in the Al-doped films. Besides, the structural defects and disorder including broken bonds, dislocations, and substoichiometric composition also form at the grain boundaries within nanosheet structure during the growth of NiO nanosheet. This finding also suggested that the Al doping causes disintegration of crystallites and leads to an increase of the compressive strain and tensile stress.

The presence of very small amount of other oxide such as Al_2O_3 or/and spinel phase on the nanosheet surface may lead to an increase of compressive strain and tensile stress in the host lattice. The increase of strain and stress in the doped NiO samples were also reported by other researchers. For instance, Dewan et al. reported that the tensile stress in Zn-doped NiO films increases with the doping concentration up to 10 at.%, which is due to substitutional defects of Zn doping in the NiO lattice [46]. Gawali et al. reported that the strain in cerium (Ce)-doped NiO film rises when doped with Ce up to 2 at.% [47]. They suggested that the increased strain is attributed to the local distortion in NiO lattice induced by ionic radii difference between Ni^{2+} and Ce^{4+} ions. Amor et al. reported that microstrain in NiO films increases when doped with cadmium (Cd) up to 2 at.% [20]. They also showed that the dislocation density of Cd-doped NiO film increased when doped at doping concentration up to 2 at.%. Similarly Mrabet et al. observed microstrain and dislocation density in NiO films upsurged when doped with lanthanum up to 4 at.% [48].

The optical properties of ANO1 to ANO7 were investigated from the transmittance spectra by UV–Vis spectroscopy measurements. The transmittance spectra of ANO1 to ANO7 deposited onto ITO glass are presented in Fig. 6. The transmission characteristics of the NiO nanosheet arrays change with different amount of Al doping. The spectra reveal that average transmittance of ANO1, ANO2, ANO3, ANO4, ANO5, ANO6, and ANO7 in the visible region (400–800 nm) are 29, 56, 88, 89, 93, 94, and 95%, respectively. The average transmittance data of the samples are summarized in Table 2. The transmission significantly increases with Al content. The pristine ANO1 sample exhibits the lowest transparency in the visible region due to the presence of large and thick NiO nanosheet arrays, which can witness noticeably in the FESEM results. This structure induces high optical scattering, which increases the transmittance path inside film and reduces the light transmittance across the film. As the Al doping increases to higher amount, the transmittance of the films increases due to thin NiO layer and small sizes of both crystallite and nanosheet, which encourages the light to pass through the films.

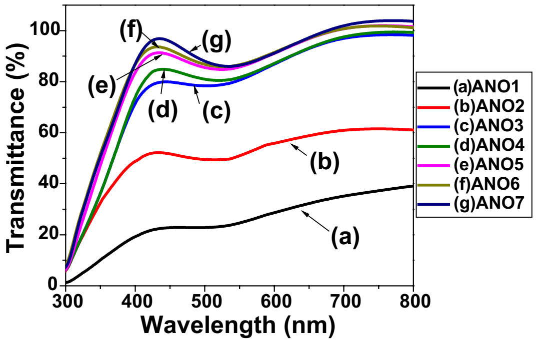

Fig. 6 The transmittance properties of ANO1 to ANO7 samples in the UV and visible region

The Davis and Mott equation is applied to estimate the optical bandgap E_g of ANO1 to ANO7 by involving the incident photon energy (hν) with the absorption coefficient as following relation:

$$ah\nu = B\left(h\nu - E_g\right)^n \tag{15}$$

here B represents a constant, and the value of n to be subjected to the transition type. For the direct allowed transitions, n = 1/2 is used, which provides excellent linear curve in the band edge region of the Tauc's plot. Therefore, the optical band gap values of the ANO1 to ANO7 are estimated using Tauc's plot by plotting $(\alpha h\nu)^2$ versus $h\nu$ and extrapolating the linear curve to discover $h\nu$ value at x-axis intercept. The Tauc's plots for the ANO1 to ANO7 samples are presented in Fig. 7. The acquired optical band gap values in terms of Al doping amounts are presented in Table 2. The result shows that the obtained band gap values are parallel with those reported for NiO films [49, 50]. This blue-shift of band gap value with the increase of Al-doping concentration might be due to the lattice contraction as evident by calculation results of lattice parameter, a and interplanar distance, d. Therefore, the interatomic spacing of NiO doped with Al at different amount is altered to small value, which causes broadening of the band gap. In addition, the smaller crystallite size induced by Al-doping may generate higher

Table 2 Optical transmittance, bandgap, electrical resistance, and resistivity of Al-doped NiO nanosheet array films

Sample	Average transmittance in the visible region (%)	Optical bandgap (eV)	Resistance (MΩ)	Resistivity (Ω m)
ANO1	29	3.747	18.7	3.97×10^{7}
ANO2	56	3.849	35.5	1.01×10^{8}
ANO3	88	3.852	44.1	3.82×10^{8}
ANO4	89	3.859	69.9	1.92×10^{9}
ANO5	93	3.872	99.5	4.53×10^{9}
ANO6	94	3.883	140.0	8.65×10^{9}
ANO7	95	3.885	207.9	2.24×10^{10}

defect incidents as suggested by dislocation densities, δ and strain/stress results, which change the electronic transition in the doped samples and lead to the blue shift of bandgap energies. The supremacy of quantum confinement effects in smaller crystallite size may also become a contributive factor in the blue shifting of the bandgap. According to Flynn et al., the filling of Al ions into Ni vacancies passivates the O dangling bonds induced by Ni vacancies [51]. This condition diminishes the defect state above the valence band maximum, which increase the energy gap between valence band and conduction band. Besides, the morphology, crystallinity, optical scattering, and degree of stoichiometry also contribute to the variation of band gap energy in the doped and Al-doped samples [52–54].

The room temperature I–V measurement plots of ANO1 to ANO7 are depicted in Fig. 8a. The samples were measured under room lighting using two-probe measurement system. The schematic of I–V measurement for ANO1 to ANO7 samples is illustrated in Fig. 8b. According to the obtained I–V measurement graph, ANO1 to ANO7 samples demonstrate the ohmic behavior with linear plots that obeys Ohm's law, which states that current through a material from one point to another point is directly proportional to the voltage between these two points. Based on the I–V plots, it can be witnessed that the current reduces as the Al doping concentration increased to 2 at.% in the voltage ranges between − 10 and 10 V. The roles of the Al-doping concentration on the film's resistivity were further investigated. The resistivity ρ of ANO1 to ANO7 samples were calculated from the gradient of the I–V measurement plots using equation below:

$$\rho = \left(\frac{V}{I}\right)\frac{A}{t} \tag{16}$$

where V, I, A, and t denote voltage, current, surface area of the electrode, and thickness, respectively. The resistance and resitivity of the ANO1 to ANO7 samples are presented in Table 2. The resistivity plot is displayed in the Fig. 9, which suggests that Al-doping increases the resistivity of the NiO nanosheet array films with respect to the Al-doping concentration up to 2 at.%. Generally, the electrical conductivity of pristine NiO is generated by the native defects, such as Ni vacancies. It is well known that pristine NiO is a charge-transfer metal oxide. The pristine NiO forms in the halite (rock salt) structure and their 3d^8 orbitals are partly filled. The electrical conduction occurs predominantly through

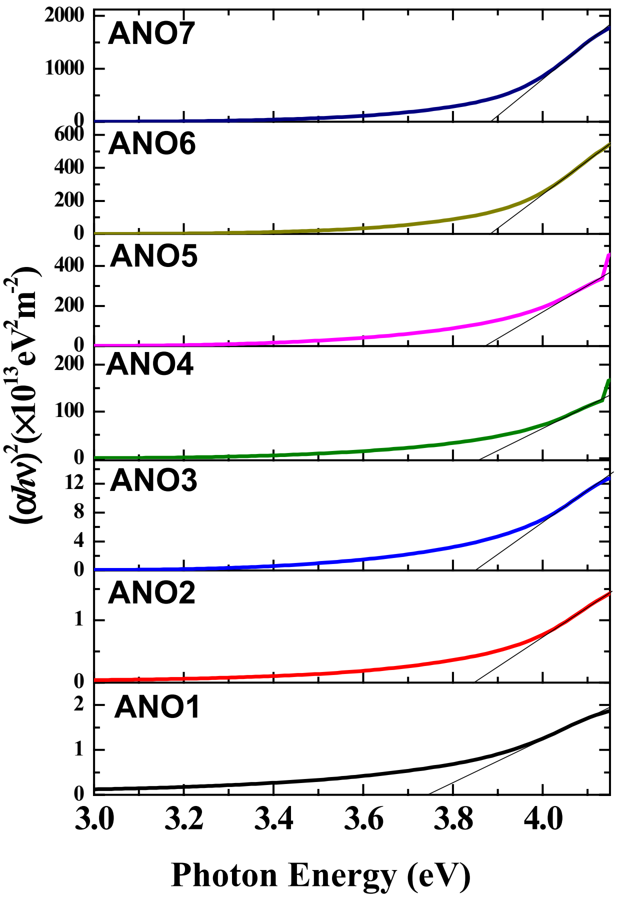

Fig. 7 The Tauc' plot for optical bandgap estimation for ANO1 to ANO7 samples

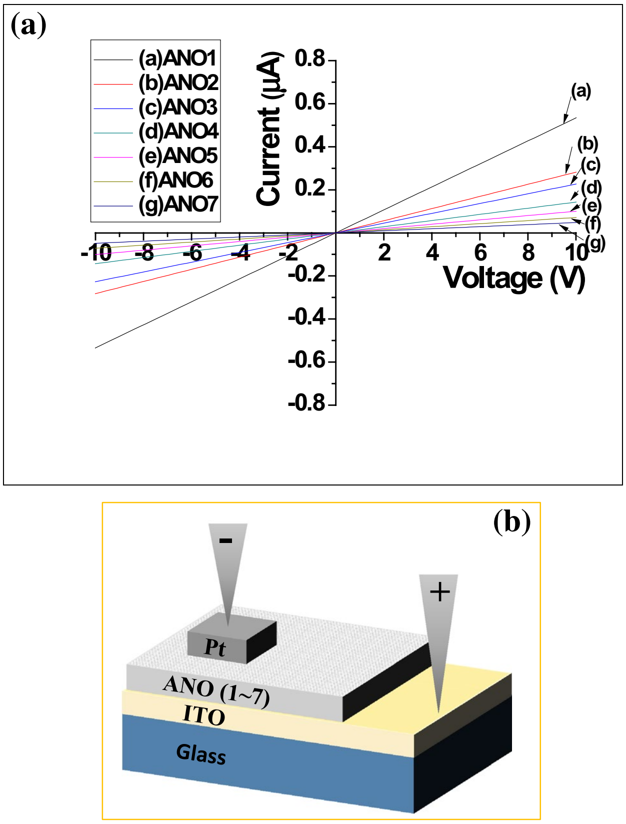

Fig. 8 **a** I–V plots of Al-doped NiO nanosheet film as a function of Al content. **b** Schematic of I–V measurement for the samples

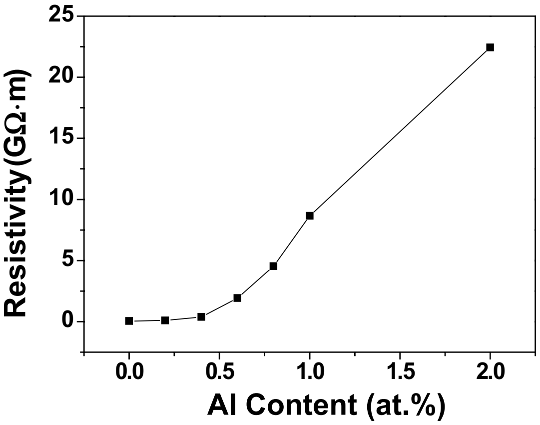

Fig. 9 The resistivity plot of Al-doped NiO nanosheet film at different Al content

hopping process of the charge carriers due to non-overlapping $3d^8$ orbitals, which forming intermittent bands. The Ni vacancies are formed through the reaction between atmospheric oxygen gases, which can be shown as follows [46]:

$$\frac{1}{2}O_2 \leftrightarrow O_O + V_{Ni}^{-} + h^{+} \tag{17}$$

In this reaction, the Ni vacancy is considered to be singly ionized, which maintain the charge neutrality of the NiO. This negatively charged and singly ionized Ni vacancy is indemnified by the emergence of hole with positive charge. The above equation suggests that the Ni vacancy defect forms NiO structure with non-stoichiometric properties and convey electrical conductivity in NiO based on hole as a carrier.

The Al doping in NiO is realized through the Al^{3+} substitution at the Ni^{2+} site. The substitution of Al^{3+} at a Ni^{2+} site in the NiO lattice can be represented by the following relations, which generates electrons by the electronic compensation and/or ionic compensation mechanisms [55]

$$Al_2O_3 \longrightarrow 2NiO2Al_{Ni}^{\cdot} + 2O_O^X + \frac{1}{2}O_2 + 2e^{-} \tag{18}$$

$$Al_2O_3 \longrightarrow 3NiO2Al_{Ni}^{\cdot} + 3O_O^X + V_{Ni}'' \tag{19}$$

Therefore, Al-doping leads to the generation of either electrons or Ni vacancies. The electron compensation mechanism in Eq. (18) reduces the hole concentration in the p-type NiO due to the generation of electrons. Consequently, the resistivity of the doped sample increases due to decreased carrier concentration. However, the Eq. (19) which represents the ionic compensation mechanism, does not affect the hole concentration in the p-type NiO. Based on the increased resistivity observed in Fig. 9 with the increased of Al dopant concentration, we believe that the electronic compensation mechanism is more feasible in this study.

The room temperature Raman spectra of ANO1 to ANO7 samples in the frequency ranges from 100 to 2000 cm^{-1} are shown in Fig. 10. The Raman spectrum of pristine ANO1 shows main vibration modes centered at 461 cm^{-1}, 496 cm^{-1}, 789 cm^{-1}, and 1093 cm^{-1} corresponding to one-phonon transverse optical (TO), one-phonon longitudinal optical (LO), two-phonon TO, and two-phonon LO stretching modes, respectively [56]. The one-phonon TO and one-phonon LO were reported to relate with structural defects in NiO lattice and the presence of these peaks are an indication that the grown NiO nanosheets contain the defects of Ni vacancy, oxygen interstitial, structural imperfections and surface-related defects [57]. In the perfect stoichiometry condition of NiO with cubic or rhombohedral structure, these one-phonon TO and one-phonon LO stretching modes are not observed as reported in literature [58, 59]. This result indicates that the synthesized NiO nanosheet structures have non-stoichiometric characteristics and possess several lattice defects, which turning the color of films into grey. When the Al-doping at different concentrations are introduced into NiO lattice as displayed by ANO2 to ANO7 samples, the peaks of one-phonon TO and one-phonon LO stretching modes are broadened and their corresponding peak positions are slightly shifted to higher Raman wavenumbers. The peak positions of ANO1 to ANO7 samples are tabulated in Table 3. These shiftings were due to integration of Al^{3+} dopant ions into NiO lattice, in which the dopant ions have higher oxidation state than Ni^{2+} cations [60, 61]. These conditions are also attributed to the structural disorder and lattice defect occurrences in the NiO structure, which are necessary to preserve neutrality of charge when the dopant ions incorporating into NiO lattice [57]. As a result, both lattice parameters and unit cell volume of Al-doped NiO nanosheet reduce, which are shown in the XRD analysis. Consequently, the bond length of Al-doped NiO nanosheet shrinks while the force constant

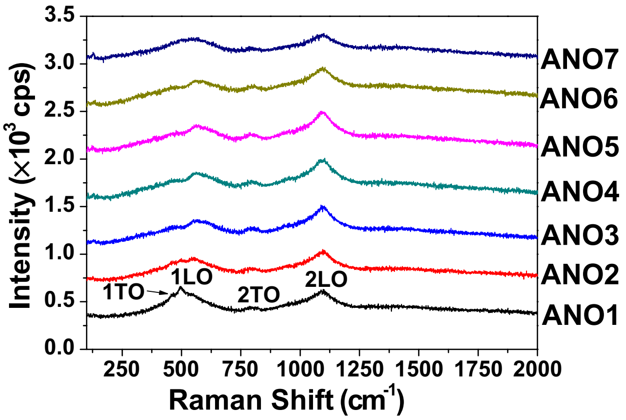

Fig. 10 Raman spectra of the grown ANO1 to ANO7 samples

Table 3 The peak positions of Raman spectra for ANO1 to ANO7 samples

Sample	One-phonon LO peak (cm^{-1})	One-phonon TO peak (cm^{-1})	Two-phonon TO peak (cm^{-1})	Two-phonon LO peak (cm^{-1})
ANO1	461	496	789	1093
ANO2	463	547	790	1095
ANO3	464	552	794	1096
ANO4	467	559	796	1097
ANO5	467	561	798	1098
ANO6	469	562	803	1098
ANO7	471	562	804	1099

of the lattice improves and this condition is translated into higher frequency of Raman vibration or higher wavenumber of the Raman shift during Raman measurement. The decreased crystallite size in the Al-doped samples may induce phonon confinement effect and shifting these first order Raman peak positions to higher vibration frequencies [43]. Moreover, it was also suggested that the one-phonon LO scattering mode arising in NiO attribute to Ni vacancy defects and the presence of Ni^{3+} cations [48, 62–65]. It can be perceived from Fig. 10 that the intensity of one-phonon LO scattering mode for ANO1 is higher than that of Al-doped samples, which are represented by ANO2 to ANO7. Hence, it can be determined that the presence of Ni^{3+} cations and Ni vacancy defects in the pristine ANO1 sample is greater compared to the Al-doped samples. This observation reinforces the previous discussion of bandgap, whereby the Al dopant is likely filled into Ni vacancy defects to reduce the Ni vacancy incidence in the process. Meanwhile, the reduced intensity of these peaks with Al doping concentration can be ascribed to the reduced growth of the NiO nanosheet after the doping process as can be observed in the FESEM images. All samples exhibit strong two-phonon LO stretching mode, which is due to the vibration of Ni–O bond. This peak intensity slightly increases when the doping concentration is increased up to 1 at.% but decreases when the concentration is increased further to 2 at.%. For the two-phonon TO stretching mode, all samples exhibit broad peaks with low intensities. The absence of two magnon (2 M) Raman mode at 1490 cm^{-1}, which typically observed in case of bulk NiO, provides an insight that the pristine and Al-doped NiO nanosheet array films show reduced coupling strength and spin correlation of antiferromagnetic characteristics. This condition is caused by small crystallite size and presence of structural disorder for both pristine and doped samples. This result suggests that the antiferromagnetic-to-paramagnetic conversion emerged in the synthesized samples.

4 Conclusion

In summary, ANO1 to ANO7 samples were successfully grown directly on ITO glass substrates at various doping concentration ranges between 0 and 2 at.% using sol–gel immersion method. FESEM observations suggested that Al-doping changes the morphological of NiO films from large and porous nanosheets to small and dense nanosheet structures at high Al concentration. The XRD analysis reveals that the prepared films have fcc NiO crystalline structure. The peaks corresponding to the (111), (200), (220), and (311) planes were observed for ANO1 sample but the intensity of these peaks reduced dramatically as the doping concentration was increased up to 2 at.%. The crystallinity of the samples declined at higher Al content, which attributed to the lattice defects induced by doping process. Subsequently, the lattice parameter and interplanar spacing decreased at high quantity of Al doping. The lattice parameter reduced from 4.1322 nm to 4.0976 nm, while the interplanar spacing reduced from 2.3857 to 2.3658 nm, when the doping concentration was increased from 0 to 2 at.%. In addition, the compressive strain, tensile stress and dislocation density rose to 1.90% (ANO1: 1.08%), 6.14 GPa (ANO1: 3.47 GPa), 5.52×10^{15} Lines/m^2 (ANO1: 3.93×10^{14} Lines/m^2), respectively, as the Al content increased to 2 at.%. The optical transmittance for the doped samples increased drastically after Al-doping particularly at high doping concentration. For Al-doped NiO samples, a blue-shift in optical bandgap from 3.747 to 3.885 eV was perceived with increasing Al content due to the lattice contraction. All samples showed linear I–V characteristics but with different resistance and resistivity values; the higher the Al content, the higher the resistance and resistivity values were recorded for the samples due to electronic compensation mechanism. The resistance values was increased from 18.7 MΩ (for ANO1) to 207.9 MΩ (for ANO7), while the resistivity values was augmented from 3.97×10^7 Ω m (for ANO1) to 2.24×10^{10} Ω m (for ANO7). The Raman analysis revealed that Al-doped samples exhibit structural defects as shown by blue-shifted phonon vibration peaks and reduced characteristic peaks of NiO.

Acknowledgement The author (M.H. Mamat) would like to thank DST of Indian Government for the ASEAN-India Research & Training Fellowship Scheme (IMRC/AISTDF/R&D/P-1/2017). The conducted research was funded by Fundemental Research Grant Scheme (FRGS) (File No: FRGS/1/2018/TK04/UITM/02/23). The authors acknowledge the supports received from the Faculty of Electrical Engineering of UiTM and Institute of Research Management and Innovation (IRMI).

References

1. H. Kheel, G.-J. Sun, J.K. Lee, A. Mirzaei, S. Choi, C. Lee, Hydrogen gas detection of Nb_2O_5 nanoparticle-decorated CuO nanorod sensors. Met. Mater. Int. **23**, 214–219 (2017)
2. S. Karunamoorthy, M. Velluchamy, Design and synthesis of bandgap tailored porous Ag/NiO nanocomposite: an effective visible light active photocatalyst for degradation of organic pollutants. J. Mater. Sci.: Mater. Electron. **29**, 20367–20382 (2018)
3. A.S. Ismail, M.H. Mamat, I.B. Shameem Banu, M.F. Malek, M.M. Yusoff, R. Mohamed, W.R.W. Ahmad, M.A.R. Abdullah, A.B. Suriani, M.K. Ahmad, M. Rusop, Modulation of Sn concentration in ZnO nanorod array: intensification on the conductivity and humidity sensing properties. J Mater Sci: Mater Electron **29**, 12076–12088 (2018)
4. Z. Li, L. Wei, Y. Liu, Y. Su, X. Dong, Y. Zhang, Facile synthesis of single-crystalline mesoporous NiO nanosheets as high-performance anode materials for Li-ion batteries. J. Mater. Sci.: Mater. Electron. **28**, 13853–13860 (2017)
5. S. Weber, T. Rath, J. Mangalam, B. Kunert, A.M. Coclite, M. Bauch, T. Dimopoulos, G. Trimmel, Investigation of NiOx-hole transport layers in triple cation perovskite solar cells. J. Mater. Sci.: Mater. Electron. **29**, 1847–1855 (2018)
6. M.H. Mamat, N.N. Hafizah, M. Rusop, Fabrication of thin, dense and small-diameter zinc oxide nanorod array-based ultraviolet photoconductive sensors with high sensitivity by catalyst-free radio frequency magnetron sputtering. Mater. Lett. **93**, 215–218 (2013)
7. S. Hussain, P. Wan, N. Aslam, G. Qiao, G. Liu, M. Wang, Ag-doped NiO porous network structure on Ni foam as electrode for supercapacitors. J. Mater. Sci.: Mater. Electron. **29**, 1759–1765 (2018)
8. T. Geng, X. Zhou, H. Wu, Facile hydrothermal synthesis $NiHPO_3{\cdot}H_2O$ nanorods, influencing factors, and transformation toward Ni–NiO composite nanostructures, catalytic properties and application in sensing for glucose. J. Mater. Sci.: Mater. Electron. **27**, 8416–8427 (2016)
9. M. Ranjbar, M.A. Taher, A. Sam, NiO nanostructures: novel solvent-less solid-state synthesis, characterization and MB photocatalytic degradation. J. Mater. Sci.: Mater. Electron. **26**, 8029–8034 (2015)
10. J. Li, J. Ma, S. Chen, J. He, Y. Huang, Characterization of calcium alginate/deacetylated konjac glucomannan blend films prepared by Ca^{2+} crosslinking and deacetylation. Food Hydrocoll. **82**, 363–369 (2018)
11. M. Cai, J. Zhu, C. Yang, R. Gao, C. Shi, J. Zhao, A parallel bicomponent TPU/PI membrane with mechanical strength enhanced isotropic interfaces used as polymer electrolyte for lithium-ion battery. Polymers **11**, 185 (2019)
12. M. Ma, Y. Yang, W. Li, R. Feng, Z. Li, P. Lyu, Y. Ma, Gold nanoparticles supported by amino groups on the surface of magnetite microspheres for the catalytic reduction of 4-nitrophenol. J. Mater. Sci. **54**, 323–334 (2019)
13. G. Wu, H. Zhang, X. Luo, L. Yang, H. Lv, Investigation and optimization of Fe/ZnFe2O4 as a Wide-band electromagnetic absorber. J. Colloid Interface Sci. **536**, 548–555 (2019)
14. G. Wu, Z. Jia, Y. Cheng, H. Zhang, X. Zhou, H. Wu, Easy synthesis of multi-shelled ZnO hollow spheres and their conversion into hedgehog-like ZnO hollow spheres with superior rate performance for lithium ion batteries. Appl. Surf. Sci. **464**, 472–478 (2019)
15. S. Liu, W. Zeng, T. Chen, Synthesis of hierarchical flower-like NiO and the influence of surfactant. Physica E **85**, 13–18 (2017)
16. S. Xi, Y. Zhu, Y. Yang, S. Jiang, Z. Tang, Facile synthesis of free-standing NiO/MnO_2 core-shell nanoflakes on carbon cloth for flexible supercapacitors. Nanoscale Res. Lett. **12**, 171 (2017)
17. H. Ren, C. Gu, S.W. Joo, J. Zhao, Y. Sun, J. Huang, Effective hydrogen gas sensor based on NiO@rGO nanocomposite. Sens. Actuator B **266**, 506–513 (2018)
18. Y. Zhao, J. Yan, Y. Huang, J. Lian, J. Qiu, J. Bao, M. Cheng, H. Xu, H. Li, K. Chen, Interfacial self-assembly of monolayer Mg-doped NiO honeycomb structured thin film with enhanced performance for gas sensing. J. Mater. Sci.: Mater. Electron. **29**, 11498–11508 (2018)
19. R. Lontio Fomekong, H.M. Tedjieukeng Kamta, J. Ngolui Lambi, D. Lahem, P. Eloy, M. Debliquy, A. Delcorte, A sub-ppm level formaldehyde gas sensor based on Zn-doped NiO prepared by a co-precipitation route. J. Alloy Compd. **731**, 1188–1196 (2018)
20. M. Ben Amor, A. Boukhachem, A. Labidi, K. Boubaker, M. Amlouk, Physical investigations on Cd doped NiO thin films along with ethanol sensing at relatively low temperature. J. Alloy Compd. **693**, 490–499 (2017)
21. C. Wang, X. Cui, J. Liu, X. Zhou, X. Cheng, P. Sun, X. Hu, X. Li, J. Zheng, G. Lu, Design of superior ethanol gas sensor based on Al-doped NiO nanorod-flowers. ACS Sens. **1**, 131–136 (2016)
22. M. Predanocy, I. Hotový, M. Čaplovičová, Structural, optical and electrical properties of sputtered NiO thin films for gas detection. Appl. Surf. Sci. **395**, 208–213 (2017)
23. S. Koussi-Daoud, O. Majerus, D. Schaming, T. Pauporté, Electrodeposition of NiO films and inverse opal organized layers from polar aprotic solvent-based electrolyte. Electrochim. Acta **219**, 638–646 (2016)
24. A.A. Akl, S.A. Mahmoud, Effect of growth temperatures on the surface morphology, optical analysis, dielectric constants, electric susceptibility, Urbach and bandgap energy of sprayed NiO thin films. Optik **172**, 783–793 (2018)
25. N. Pal, S. Banerjee, A. Bhaumik, A facile route for the syntheses of Ni(OH)2 and NiO nanostructures as potential candidates for non-enzymatic glucose sensor. J. Colloid Interface Sci. **516**, 121–127 (2018)
26. S. Wang, D. Huang, S. Xu, W. Jiang, T. Wang, J. Hu, N. Hu, Y. Su, Y. Zhang, Z. Yang, Two-dimensional NiO nanosheets with enhanced room temperature NO_2 sensing performance via Al doping. Phys. Chem. Chem. Phys. **19**, 19043–19049 (2017)
27. Q. Zhou, A. Umar, E.M. Sodki, A. Amine, L. Xu, Y. Gui, A.A. Ibrahim, R. Kumar, S. Baskoutas, Fabrication and characterization of highly sensitive and selective sensors based on porous NiO nanodisks. Sens. Actuator B **259**, 604–615 (2018)
28. S.K. Meher, P. Justin, G. Rao, Nanoscale morphology dependent pseudocapacitance of NiO: influence of intercalating anions during synthesis. Nanoscale **3**, 683–692 (2011)
29. N.D. Hoa, P. Van Tong, C.M. Hung, N. Van Duy, N. Van Hieu, Urea mediated synthesis of $Ni(OH)_2$ nanowires and their conversion into NiO nanostructure for hydrogen gas-sensing application. Int. J. Hydrogen Energy **43**, 9446–9453 (2018)
30. C. Mallika, A.M. Edwin Suresh Raj, K.S. Nagaraja, O.M. Sreedharan, Use of SnO for the determination of standard Gibbs energy of formation of SnO2 by oxide electrolyte measurements. Thermochim. Acta. **371**, 95–101 (2001)
31. M. Masoumi, D.M. Cupid, T.L. Reichmann, K. Chang, D. Music, J.M. Schneider, H.J. Seifert, Enthalpies of formation of layered $LiNi_xMn_xCo_{1-2x}O_2$ $(0 \le x \le 0.5)$ compounds as lithium ion battery cathode materials. Int. J. Mater. Res. **108**, 869–878 (2017)
32. S. Phapale, R. Mishra, D. Das, Standard enthalpy of formation and heat capacity of compounds in the pseudo-binary Bi_2O_3–Fe_2O_3 system. J. Nucl. Mater. **373**, 137–141 (2008)
33. S.-Y. Kuo, W.-C. Chen, F.-I. Lai, C.-P. Cheng, H.-C. Kuo, S.-C. Wang, W.-F. Hsieh, Effects of doping concentration and annealing temperature on properties of highly-oriented Al-doped ZnO films. J. Cryst. Growth **287**, 78–84 (2006)

34. Z. Wu, Z. Zou, J. Huang, F. Gao, Fe-doped NiO mesoporous nanosheets array for highly efficient overall water splitting. J. Catal. **358**, 243–252 (2018)
35. S. Kerli, U. Alver, H. Yaykaşlı, Investigation of the properties of In doped NiO films. Appl. Surf. Sci. **318**, 164–167 (2014)
36. C. Wang, J. Liu, Q. Yang, P. Sun, Y. Gao, F. Liu, J. Zheng, G. Lu, Ultrasensitive and low detection limit of acetone gas sensor based on W-doped NiO hierarchical nanostructure. Sens. Actuator B **220**, 59–67 (2015)
37. H. Gao, Q. Yu, S. Zhang, T. Wang, P. Sun, H. Lu, F. Liu, X. Yan, F. Liu, X. Liang, Y. Gao, G. Lu, Nanosheet-assembled NiO microspheres modified by Sn^{2+} ions isovalent interstitial doping for xylene gas sensors. Sens. Actuator B **269**, 210–222 (2018)
38. C. Feng, Z. Jiang, B. Chen, P. Cheng, Y. Wang, C. Huang, Aluminum-doped NiO nanofibers as chemical sensors for selective and sensitive methanol detection. Anal. Methods **11**, 575–581 (2019)
39. F. Lin, D. Nordlund, T.-C. Weng, R.G. Moore, D.T. Gillaspie, A.C. Dillon, R.M. Richards, C. Engtrakul, Hole doping in Al-containing nickel oxide materials to improve electrochromic performance. ACS Appl. Mater. Interfaces **5**, 301–309 (2013)
40. H. Gao, Q. Yu, S. Zhang, T. Wang, P. Sun, H. Lu, F. Liu, X. Yan, F. Liu, X. Liang, Y. Gao, G. Lu, Nanosheet-assembled NiO microspheres modified by Sn^{2+} ions isovalent interstitial doping for xylene gas sensors. Sens. Actuator B **269**, 210–222 (2018)
41. M.H. Mamat, M.Z. Sahdan, Z. Khusaimi, A.Z. Ahmed, S. Abdullah, M. Rusop, Influence of doping concentrations on the aluminum doped zinc oxide thin films properties for ultraviolet photoconductive sensor applications. Opt. Mater. **32**, 696–699 (2010)
42. K.N. Patel, M.P. Deshpande, K. Chauhan, P. Rajput, V.P. Gujarati, S. Pandya, V. Sathe, S.H. Chaki, Effect of Mn doping concentration on structural, vibrational and magnetic properties of NiO nanoparticles. Adv. Powder Technol. **29**, 2394–2403 (2018)
43. K.N. Patel, M.P. Deshpande, V.P. Gujarati, S. Pandya, V. Sathe, S.H. Chaki, Structural and optical analysis of Fe doped NiO nanoparticles synthesized by chemical precipitation route. Mat. Res. Bull. **106**, 187–196 (2018)
44. M.A. Rahman, R. Radhakrishnan, R. Gopalakrishnan, Structural, optical, magnetic and antibacterial properties of Nd doped NiO nanoparticles prepared by co-precipitation method. J. Alloy Compd. **742**, 421–429 (2018)
45. A. Mallikarjuna Reddy, A. Sivasankar Reddy, P. Sreedhara Reddy, Thickness dependent properties of nickel oxide thin films deposited by dc reactive magnetron sputtering. Vacuum **85**, 949–954 (2011)
46. S. Dewan, M. Tomar, R.P. Tandon, V. Gupta, Zn doping induced conductivity transformation in NiO films for realization of p-n homo junction diode. J. Appl. Phys. **121**, 215307 (2017)
47. S.R. Gawali, V.L. Patil, V.G. Deonikar, S.S. Patil, D.R. Patil, P.S. Patil, J. Pant, Ce doped NiO nanoparticles as selective NO_2 gas sensor. J. Phys. Chem. Solids **114**, 28–35 (2018)
48. C. Mrabet, M.B. Amor, A. Boukhachem, M. Amlouk, T. Manoubi, Physical properties of La-doped NiO sprayed thin films for optoelectronic and sensor applications. Ceram. Int. **42**, 5963–5978 (2016)
49. Y. Akaltun, T. Çayır, Fabrication and characterization of NiO thin films prepared by SILAR method. J. Alloy Compd. **625**, 144–148 (2015)
50. L. Umaralikhan, M.J.M. Jaffar, X-ray broadening and optical properties of NiO nanoparticles prepared via co-precipitation method by varying temperature. Iran. J. Sci. Technol. Trans. A Sci. **42**, 2345–2348 (2018)
51. C.J. Flynn, S.M. McCullough, E. Oh, L. Li, C.C. Mercado, B.H. Farnum, W. Li, C.L. Donley, W. You, A.J. Nozik, J.R. McBride, T.J. Meyer, Y. Kanai, J.F. Cahoon, Site-selective passivation of defects in NiO solar photocathodes by targeted atomic deposition. ACS Appl. Mater. Interfaces **8**, 4754–4761 (2016)
52. A. Yazdani, H. Zafarkish, K. Rahimi, The variation of Eg-shape dependence of NiO nanoparticles by the variation of annealing temperature. Mater. Sci. Semicond. Process. **74**, 225–231 (2018)
53. M.F. Malek, M.H. Mamat, Z. Khusaimi, M.Z. Sahdan, M.Z. Musa, A.R. Zainun, A.B. Suriani, N.M. Sin, S.A. Hamid, M. Rusop, Sonicated sol–gel preparation of nanoparticulate ZnO thin films with various deposition speeds: the highly preferred c-axis (002) orientation enhances the final properties. J. Alloy. Compd. **582**, 12–21 (2014)
54. M.F. Malek, M.H. Mamat, M.Z. Musa, T. Soga, S.A. Rahman, S.A.H. Alrokayan, H.A. Khan, M. Rusop, Metamorphosis of strain/stress on optical band gap energy of ZAO thin films via manipulation of thermal annealing process. J. Lumin. **160**, 165–175 (2015)
55. C. Wang, J. Liu, Q. Yang, P. Sun, Y. Gao, F. Liu, J. Zheng, G. Lu, Ultrasensitive and low detection limit of acetone gas sensor based on W-doped NiO hierarchical nanostructure. Sens. Actuator B **220**, 59–67 (2015)
56. P. Bose, S. Ghosh, S. Basak, M.K. Naskar, A facile synthesis of mesoporous NiO nanosheets and their application in CO oxidation. J. Asian Ceram. Soc. **4**, 1–5 (2016)
57. Z. Wang, H. Zhou, D. Han, F. Gu, Electron compensation in p-type 3DOM NiO by Sn doping for enhanced formaldehyde sensing performance. J. Mater. Chem. C **5**, 3254–3263 (2017)
58. P. Ravikumar, B. Kisan, A. Perumal, Enhanced room temperature ferromagnetism in antiferromagnetic NiO nanoparticles. AIP Adv. **5**, 087116 (2015)
59. S. Liu, J. Jia, J. Wang, S. Liu, X. Wang, H. Song, X. Hu, Synthesis of Fe-doped NiO nanofibers using electrospinning method and their ferromagnetic properties. J. Magn. Magn. Mater. **324**, 2070–2074 (2012)
60. Y. Ji-Wook, K. Hyo-Joong, K. Il-Doo, L. Jong-Heun, Electronic sensitization of the response to C_2H_5OH of p-type NiO nanofibers by Fe doping. Nanotechnology **24**, 444005 (2013)
61. L. Xiu, T. Jian-Feng, E.H. Yan, H. Xin-Tang, Microwave-assisted synthesis of Fe-doped NiO nanofoams assembled by porous nanosheets for fast response and recovery gas sensors. Mater. Res. Exp. **4**, 045015 (2017)
62. D.Y. Jiang, J.M. Qin, X. Wang, S. Gao, Q.C. Liang, J.X. Zhao, Optical properties of NiO thin films fabricated by electron beam evaporation. Vacuum **86**, 1083–1086 (2012)
63. C.A. Melendres, S. Xu, In situ laser Raman spectroscopic study of anodic corrosion films on nickel and cobalt. J. Electrochem. Soc. **131**, 2239–2243 (1984)
64. D.A. Wruck, M. Rubin, Structure and electronic properties of electrochromic NiO films. J. Electrochem. Soc. **140**, 1097–1104 (1993)
65. S.H. Lee, H.M. Cheong, N.G. Park, C.E. Tracy, A. Mascarenhas, D.K. Benson, S.K. Deb, Raman spectroscopic studies of Ni-W oxide thin films. Solid State Ion. **140**, 135–139 (2001)